

SMITH DIAGRAM FOR LOW REYNOLDS NUMBER AXIAL FAN ROTORS

R. Corralejo - P. Harley

Dyson Ltd., Malmesbury, UK
raul.corralejo@dyson.com

ABSTRACT

Compressor operation at low Reynolds numbers is commonly associated with a loss increase. A semi-analytical approach was used to investigate this region of the design spectrum. To do this, an axial rotor with constant diameter endwalls was non-dimensionalised to understand the influence of different design parameters independently. Smith diagrams showing contours of efficiency on a plot of flow coefficient versus stage loading coefficient were produced at low and high Reynolds numbers. The results showed not only lower levels of efficiency at low Reynolds numbers but a much narrower high efficiency island, with losses rapidly increasing as the design moved away from the high efficiency region. Several points in the Smith diagram were selected, dimensionalised and simulated using CFD with and without a transition model. Good agreement between the CFD and the model was found, with discrepancies increasing towards low efficiency regions. Meanline correlations for the low Reynolds number regime were also provided.

KEYWORDS: Axial fan, Reynolds number, Smith diagram, loss, deviation.

NOMENCLATURE

AR	Aspect ratio ($= h/c$)	$\eta_{T/T}$	T/T isentropic efficiency (Eq. 18)
c	Chord	$\Delta\eta$	Loss of efficiency
C_D	Dissipation coefficient	ρ	Density
C_d	Discharge coefficient	σ	Solidity
DF	Diffusion factor (Eq. 19)	ϕ	Flow coefficient ($= M_{ax}/M_u$)
g	Tip gap	χ	Blade angle (meridional ref.)
h	Blade span height	$\Delta\chi$	Blade camber angle ($= \chi_1 - \chi_2$)
i	Incidence ($= \beta_1 - \chi_1$)	ψ	Stage loading coefficient ($= M_{\theta 2}/M_u$)
M	Mach number	Ω	Rotational speed
\dot{m}	Mass flow rate	ω	Total pressure loss coefficient
N_b	Number of blades	Sub- and superscripts	
P	Pressure	1, 2	Rotor inlet, outlet
r	Radius	t	Tip / Stagnation quantity
Re	Chord-based Reynolds number	h	Hub
r_h/r_t	Hub-to-tip ratio	m	Midspan
\bar{S}	Non-dimensional passage area	ax	Axial
T	Temperature	s	Suction surface
\bar{V}	Non-dimensional local velocity	p	Pressure surface
\bar{z}	Non-dimensional chord-wise length	θ	Tangential
β	Relative flow angle (meridional ref.)	u	Blade speed
δ	Flow deviation ($= \beta_2 - \chi_2$)	r	Relative frame of reference
ϵ	Tip gap-to-span ratio ($= g/h$)	*	Modified

INTRODUCTION

Small compression systems are widely used in household appliances to move air. The low flow velocities combined with the small scale entails that the chord-based Reynolds number is low, which is commonly associated with higher levels of loss (Maffioli et al., 2015). Efficiency is a key performance metric for compressors and for this reason it is important to understand the effect of Reynolds number on it (Casey, 1985; Pelz and Stonjek, 2013).

The increase of loss as the Reynolds number decreases (Fig. 1) is due to a number of different mechanisms:

- Boundary layer dissipation grows with decreasing Reynolds number (Denton, 1993).
- Boundary layers get thicker, increasing blade deviation and hence lessening the amount of energy transferred into the flow (Japikse and Baines, 1997).
- Blade boundary layers may remain laminar for longer portions of the blade, which are more prone to separation and incur higher losses if this occurs (Japikse and Baines, 1997).

Preliminary design of an axial compressor stage typically relies on meanline methods, which employ empirical and/or semi-empirical correlations to estimate the different losses present in a turbomachinery stage. Typically, by sweeping through a number of design parameters, a geometry is identified which best suits the machine requirements. Parameters such as the flow and stage loading coefficient are important since they define the size and shape of a compressor; an ill-informed selection at the initial stages of design can lead to poor efficiency, irrespective of the design effort invested later. The majority of loss correlations are based on high Reynolds number turbomachines and it has been shown in open literature that some loss mechanisms increase as the Reynolds number decreases (Maffioli et al., 2015). It is therefore unclear whether the performance prediction from the aforementioned correlations is accurate for low Reynolds numbers and most importantly, whether the optimum design parameters calculated at the meanline level remain valid for low Reynolds number axial fans.

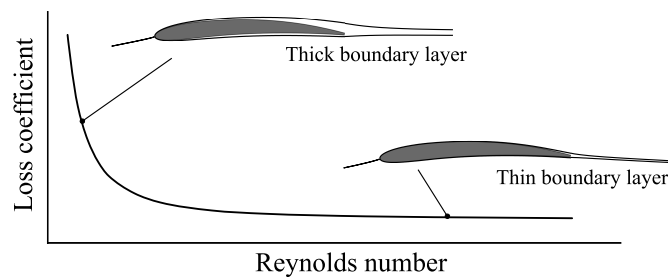


Figure 1: **Effect of Reynolds number on loss coefficient**

Possible ways of assessing the previous points include large design of experiment (DOE) studies either numerically or experimentally; however, both techniques are very resource intensive. Since it was deemed important to have a fast low cost calculation model, another approach was considered; it consisted of modelling the rotor losses separately based on physical processes and adding them together to calculate the overall rotor efficiency. Such a method allows a loss breakdown and informs where the effort should be invested to further improve the efficiency. Nevertheless, its accuracy depends on the validity of the loss models used and further validation was needed.

A number of studies that incorporate this methodology can be found in the literature. Most of them employ MISES (Drela and Youngren, 2008) as their numerical solver. MISES is a

coupled Euler/integral boundary layer quasi-3D blade-to-blade solver, with the AGS (Abu-Ghannam/Shaw) transition model implemented, and has been proven to accurately predict compressor cascade performance at low Reynolds numbers (Schreiber et al., 2004). In Fitzgerald (2002), a meanline code using data from MISES to compute the loss coefficient and the deviation angle was coupled with a newly developed model to calculate the double tip leakage losses and blockage; this tip model was an improvement over Denton's tip leakage model (Denton, 1993), but still used a CFD dataset as empirical input to refine the model. DiOrio (2012) employed MISES to assess the effect of the Reynolds number on a turbofan high pressure compressor; a drop of around 5 points in total-to-total efficiency was reported from changing the baseline design operating Reynolds number from $Re = 10^6$ to $Re = 10^5$. Maffioli et al. (2015) carried out a parametric study on the influence of profile parameters on profile losses using MISES to get a high performing low Reynolds number blade. A Smith chart based on the rotor profile losses was generated, which showed that the peak efficiency was located at values of the flow coefficient greater than 0.6. Finally, Hall (2011) investigated the stage efficiency upper limits for an axial compressor and turbine; this means that only the losses that cannot be eliminated were considered (skin friction on wetted surfaces, mixing out of wakes and mixing of tip leakage). Representative design velocity distributions with turbulent boundary layers were used to calculate the losses; the Reynolds number selected was $Re = 5 \cdot 10^5$, typical of a large scale compressor. A Smith diagram for an axial compressor stage was produced, showing maximum efficiency in the region of flow coefficients between 0.3 and 0.7.

The present research builds upon the work of Hall (2011) and Maffioli et al. (2015), extends the work of the former to the low Reynolds number domain using real profiles rather than velocity distributions and of the latter to include extra loss sources into a more realistic model. The paper focuses primarily on the flow and loading coefficient effect on the rotor efficiency.

METHODOLOGY

This section describes the procedure followed to obtain Smith diagrams for both low and high Reynolds numbers. To achieve this, a profile generator was used to generate a batch of different flow and loading coefficient midspan profiles, which were simulated using MISES. A free vortex design was used to produce the blade profiles at the hub and tip regions, these profiles were simulated in MISES and semi-analytical equations applied to the 2D solutions to take into account the endwall and tip leakage losses. Finally, several points on the low Reynolds Smith diagram were selected for further comparison with CFD.

MISES Methodology

The physical loss mechanisms behind the loss of efficiency in a compressor according to Denton (1993) are due to irreversibility in the following fluid dynamic processes:

- Viscous friction in either boundary layers or free shear layers.
- Heat transfer across finite temperature differences.
- Non-equilibrium processes such as very rapid expansions or shock waves.

In this study, the Mach number was assumed to be subsonic and the flow adiabatic. Hence, the only loss mechanisms were due to viscous dissipation within boundary layers, the mixing of wakes and the mixing of the leakage flow with the main flow. Therefore, the main loss mechanisms were divided into profile, tip leakage and endwall losses (Denton, 1993). Profile losses (also referred to as 2D losses) are the losses generated on the blade sections which are far away

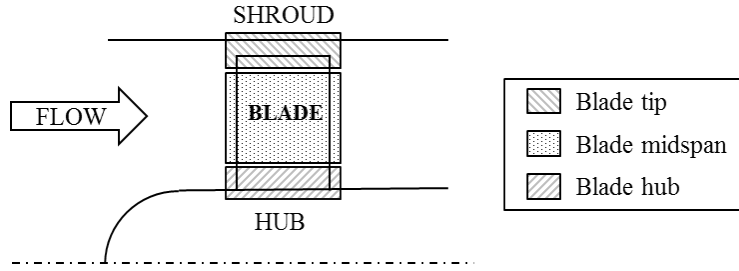


Figure 2: **Schematic of an axial rotor fan blade with sectional loss regions**

from the endwalls; they are comprised of the entropy generated in the boundary layers and wake mixing. Endwall losses may also be called secondary losses and they are a combination of the endwall boundary layer dissipation and the losses due to the interaction of the secondary flows and the blade row. The secondary flows are geometry dependent and they are a combination of many factors. Tip leakage losses arise from the dissipation of the tip leakage vortex. Tip leakage vortices are formed when flow crosses the tip gap from the pressure surface to the suction surface due to the pressure difference.

The performance metric of interest was the total-to-total efficiency. The reason behind this choice compared to the total-to-static efficiency, was that this efficiency represents the maximum achievable. For simplicity, a single rotor was investigated; however, this method could be extended to a more general configuration of a rotor and a stator. In order to calculate the total-to-total efficiency of the rotor, a similar approach to the work of Hall (2011) was followed. A rotor fan blade of parallel endwalls was divided into three different sections (hub, midspan and tip) in order to capture the three aforementioned loss mechanisms (Fig. 2). However, not in-line with Hall's work (where the author used typical blade-to-blade velocity distributions), this work employed 2D simulation data from real profiles. The efficiency loss ($\Delta\eta$) due to the three different loss mechanisms (profile, endwall and tip leakage) was calculated by modelling the entropy generation processes separately and finally added together to yield a single rotor efficiency value.

To fully determine a Smith diagram, a number of machine characteristics are to be kept constant. In order for this work to be applicable to a wide variety of machines (regardless of their physical dimensions), all the geometrical variables were non-dimensionalised. These were namely: midspan chord-based Reynolds number (Re_m), midspan relative inlet Mach number (M_{1m}^*), turbulence intensity, incidence angle (i), aspect ratio (AR), hub-to-tip ratio (r_h/r_t) and tip gap-to-span ratio (ϵ). This means that each point in the chart would correspond to a different compressor performing at a different operating point, each of them working at its design point. Such an approach allowed understanding of the effect of the separate non-dimensional parameters independently of each other. Typical non-dimensional axial fan design numbers were selected, except for the Mach number that is illustrative of a low speed machine (Fig. 3). The Reynolds number effect was the main variable of interest in this study, although this model allows the investigation of the impact of other non-dimensional variables on the efficiency.

An in-house profile generator specifically tailored for the creation of turbomachinery profiles was used to produce the aerofoil geometries. This profile generator was based on the CST (Class-Shape Transformation) method developed by Kulfan and Bussioletti (2006). The profiles consisted of a thickness distribution (which was kept constant for this study) added perpendicularly to a circular camberline. Maffioli et al. (2015) investigated high-performing low Reynolds number profiles and concluded that maximum thickness located near the leading edge yielded

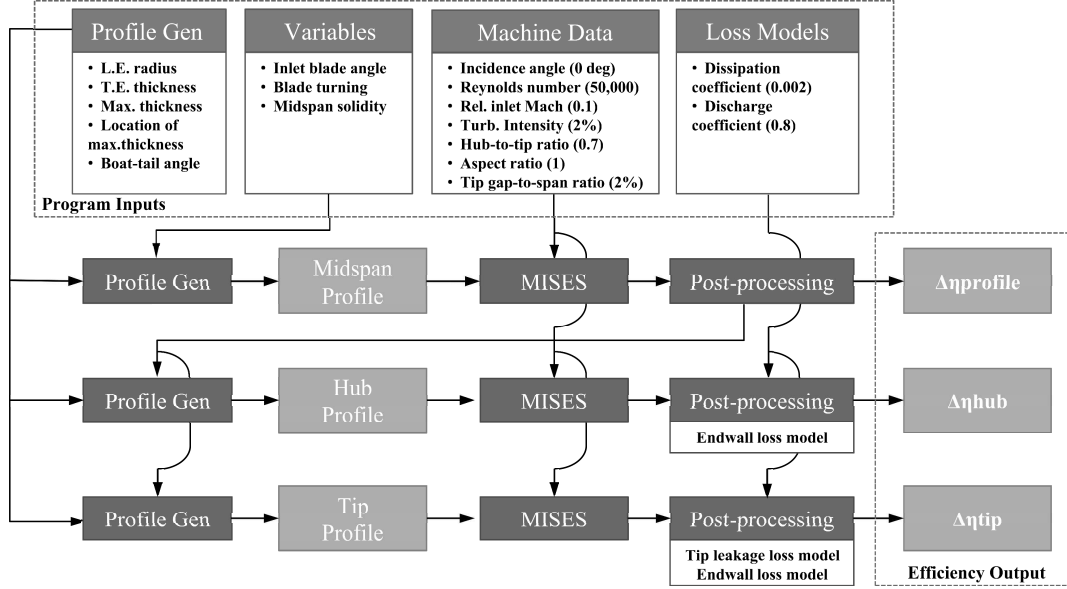


Figure 3: **Model simulation flow structure**

lower loss coefficients. Therefore, front-thickened profiles were used throughout the study. The inputs non-dimensionalised by the chord were leading edge radius, trailing edge thickness, maximum thickness, location of maximum thickness and boat-tail angle (Fig. 3).

Several parameters were allowed to be varied in order to change the flow and stage loading coefficients. They were namely the inlet blade angle (χ_1), blade camber angle ($\Delta\chi$) and midspan solidity (σ_m).

In order to manage the data and the workflow efficiently, the framework OpenMDAO (Open-source Multidisciplinary Design, Analysis, and Optimization) developed by Gray et al. (2010) was used in Python to link the data between the different pre and post-processing scripts. The structure of the process is shown in Fig. 3.

A midspan profile was created using the profile generator and simulated in MISES. It outputted a number of variables, namely total pressure loss coefficient ($\omega = (P_{1t}^r - P_{2t}^r)/(P_{1t}^r - P_1^r)$), velocity triangles, velocity distributions across the passage and outside of the boundary layer. Outputs from MISES are in the relative frame of reference and non-dimensional (given via ratios or dimensionless quantities). The reference quantities for non-dimensionalisation are: the blade chord (c) for non-dimensional lengths, the inlet local speed of sound for Mach numbers and the inlet stagnation speed of sound in the relative frame for non-dimensional velocities (Drela and Youngren, 2008). The midspan velocity triangles output from MISES were used to calculate the flow coefficient ($\phi_m = M_{ax}/M_u$) and stage loading coefficient ($\psi_m = M_{\theta 2}/M_u$) of the fan. Note that when dimensionalised, the previous definitions are equivalent to the standard axial fan definitions of flow and stage loading coefficients based on the velocities. The axial flow velocity was assumed to be the same at the inlet and the outlet, the incoming flow was axial and the flow was considered incompressible ($M^r < 0.3$).

From the definition of isentropic efficiency and using isentropic flow equations the relationship between the loss of efficiency due to profile losses ($\Delta\eta_{profile}$) and the total pressure loss coefficient (ω) was deduced.

$$\Delta\eta_{profile} = \frac{1 - \frac{T_{1t}}{T_{2t}} \cdot \left(\frac{P_{2t}}{P_{1t}}\right)^{\frac{\gamma-1}{\gamma}}}{1 - \frac{T_{1t}}{T_{2t}}} \quad (1)$$

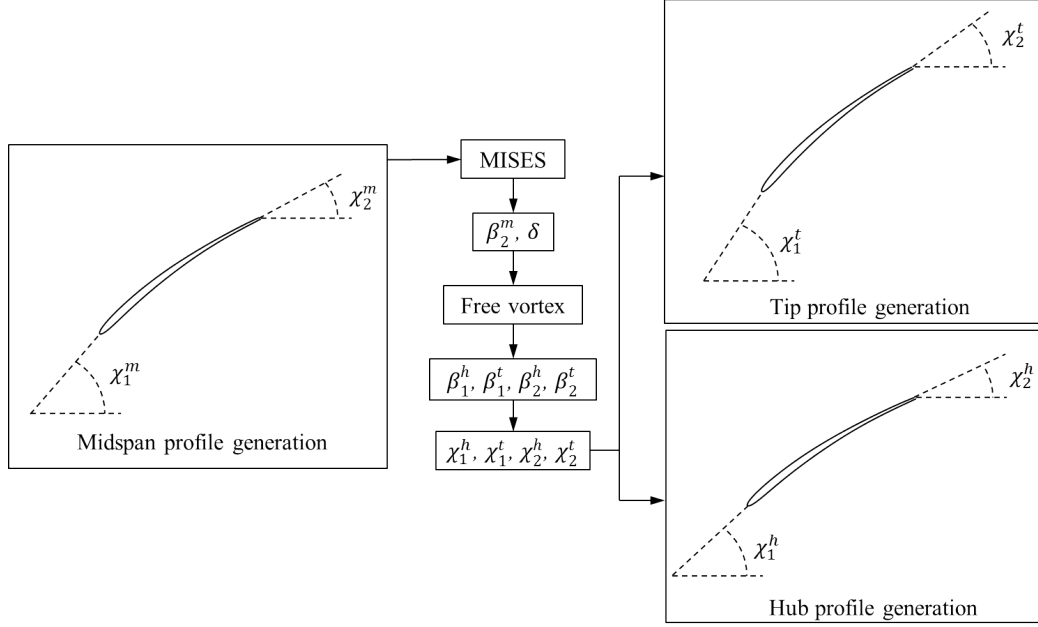


Figure 4: **Blade generation structure**

The blade generation process is summarised in Fig. 4. A free vortex design was applied along the blade span for simplicity, since it entails constant axial velocity after the blade row and constant specific work distribution from hub to tip. The hub-to-tip ratio (r_h/r_t) was employed to calculate the inlet and outlet flow angles at the hub and tip sections. In order to calculate the outlet blade angles at those sections, the deviation was assumed to be constant along the span and equal to that at the midspan; this means an underprediction at the hub and an overprediction at the tip, which is expected to compensate their effects. The chord was also considered constant along the blade. Hence, solidities, Reynolds numbers and Mach numbers were calculated as follows and the profiles generated simulated in MISES. Here the subscript x may denote either the hub or the tip variable.

$$\phi_h = 0.5 \cdot \phi_m (1 + 1/(r_h/r_t)) \quad (2)$$

$$\sigma_h = 0.5 \cdot \sigma_m (1 + 1/(r_h/r_t)) \quad (3)$$

$$\phi_t = 0.5 \cdot \phi_m (1 + r_h/r_t) \quad (4)$$

$$\sigma_t = 0.5 \cdot \sigma_m (1 + r_h/r_t) \quad (5)$$

$$M_{1x}^r = M_{1m}^r \sqrt{\frac{1 + 1/\phi_x^2}{1 + 1/\phi_m^2}} \quad (6)$$

$$Re_x = Re_m \sqrt{\frac{1 + 1/\phi_x^2}{1 + 1/\phi_m^2}} \quad (7)$$

Following the work of Hall (2011), only the dissipation due to the endwall boundary layers was taken into account for the endwall losses. The passage velocity distribution was obtained at the hub and the tip locations and integrated with a constant dissipation coefficient typical of

a turbulent boundary layer ($C_D = 0.002$). The loss of efficiency due to the endwall boundary layer can be expressed as:

$$\Delta\eta_{endwall} = \frac{\phi_m^2 C_D \sigma_m}{\psi_m (AR) M_{ax}^3} \iint \bar{V}^3 d\bar{S} \quad (8)$$

In Eq. 8, \bar{V} denoted the non-dimensional velocity across the blade passage, M_{ax} was the local axial Mach number (either at the hub or at the tip) and \bar{S} , the passage area non-dimensionalised by c^2 . Note the difference between \bar{V} and M ; the former is non-dimensionalised by the stagnation speed of sound in the relative frame and the latter by the local speed of sound. The variables written with the subscript m were the values calculated at the midspan. The hub wall was considered to be rotating with the blades, while the shroud was stationary. Since the passage velocity distribution was obtained in the relative frame, the tip passage velocities needed to be transformed into the absolute frame of reference to calculate the integral.

The pressure distribution at the tip's suction and pressure surfaces was employed in Denton's tip leakage model (Denton, 1993) to calculate the tip leakage contribution to the loss of efficiency. However, Denton makes the assumption that the Mach number at which the leakage flow mixing takes place is the same as that of the mainstream flow on the suction surface. That assumption has not been made in this study, which leads to a slightly different equation for the tip leakage loss of efficiency:

$$\Delta\eta_{tipleak} = \frac{\phi_m^2}{\psi_m} \left[\frac{1 + \frac{\gamma-1}{2} M_2^2}{1 + \frac{\gamma-1}{2} M_2^2} \right] \left[\frac{\epsilon \sigma_m C_d}{M_{ax}^3} \right] \int_0^1 \left(1 + \frac{\gamma-1}{2} M_s^2 \right) \bar{V}_s^2 \left(1 - \frac{\bar{V}_p}{\bar{V}_s} \right) \sqrt{\bar{V}_s^2 - \bar{V}_p^2} d\bar{z} \quad (9)$$

The discharge coefficient through the tip gap was taken as $C_d = 0.8$ (Denton, 1993). The subscripts p and s indicate whether the values are taken at the pressure or the suction surface respectively. And \bar{z} is the chordwise length non-dimensionalised by the blade chord (c).

The loss of efficiency contributed by profile losses, hub endwall losses, tip endwall losses and tip leakage losses were summed to calculate the overall total-to-total rotor efficiency:

$$\eta_{T/T} = 1 - (\Delta\eta_{profile} + \Delta\eta_{endwall}^{hub} + \Delta\eta_{endwall}^{tip} + \Delta\eta_{tipleak}) \quad (10)$$

A full factorial design of three variables (χ_1 , $\Delta\chi$ and σ_m) was carried out to change the flow and stage loading coefficients. The inlet blade angle (χ_1) was varied between 45° and 77° , the blade camber angle ($\Delta\chi$) between 0° and 75° and the midspan solidity (σ_m) between 0.65 and 2. All the points simulated, when represented in a 3D scatter plot where the x-axis was the flow coefficient, the y-axis was the stage loading coefficient and the z-axis was the total-to-total efficiency, formed a cloud of points. In order to retrieve the Smith diagram, which is the 2D plot of total-to-total efficiency contours on a graph where the x-axis is the flow coefficient and the y-axis is the stage loading coefficient, a filter to capture the best points in terms of efficiency was used. This filter divided the flow and stage loading coefficients in segments, creating a grid. The highest efficiency point inside each square of the grid was selected and by doing this, only the optimum designs were chosen to build the Smith diagrams.

CFD Methodology

Several points in the low Reynolds Smith diagram were chosen for further 3D CFD analysis. The blade profile sections previously generated for the model were dimensionalised and

imported in ANSYS TurboGrid. Since the flow was incompressible, for simplicity the density has been taken as the stagnation density and the temperature as the stagnation temperature. The equations used to dimensionalise the geometry to keep the machine characteristics constant were the following:

$$c = \frac{\mu R e_m}{\rho M_{1m}^r \sqrt{\gamma R T_1}} \quad (11)$$

$$h = AR \cdot c \quad (12)$$

$$r_m = (h/2)(1 + r_h/r_t)/(1 - r_h/r_t) \quad (13)$$

$$N_b = 2\pi r_m \sigma_m / c \quad (14)$$

$$g = \epsilon \cdot h \quad (15)$$

The hub (r_h) and tip radius (r_t) were easily calculated from the midspan radius (r_m) and the blade height (h). The number of blades (N_b) was rounded to the nearest integer. R , γ and μ are gas constant, specific heat ratio and dynamic viscosity of air respectively.

The boundary conditions imposed were the inlet total pressure (101,325 Pa), inlet total temperature (293 K) and mass flow at the outlet. The mass flow rate (\dot{m}) and rotational speed (Ω) were given by the equations:

$$\dot{m} = 2\rho\pi h\phi_m\Omega r_m^2 \quad (16)$$

$$\Omega = M_{1m}^r \sin \beta_1 \sqrt{\gamma R T_1} / r_m \quad (17)$$

The mesh was generated in TurboGrid using typical settings based on experience to get a y^+ of around 1 (Fig. 5). The inlet was located $0.3c$ upstream of the leading edge of the blade and the outlet was one c downstream of the trailing edge. The mesh was divided in two different domains, from the inlet until $0.75c$ downstream of the trailing edge, where the reference frame was rotating and the rest of the mesh was stationary. The interface between the two domains was a mixing plane.

The CFD simulations were completed using ANSYS CFX. Two turbulence models were tested, the first was the standard $k - \omega$ SST and the second included the $\gamma - \theta$ transition model. Since a significant portion of the blade boundary layer was expected to be laminar, the simulation setups were selected in order to understand any differences in the way boundary layers are

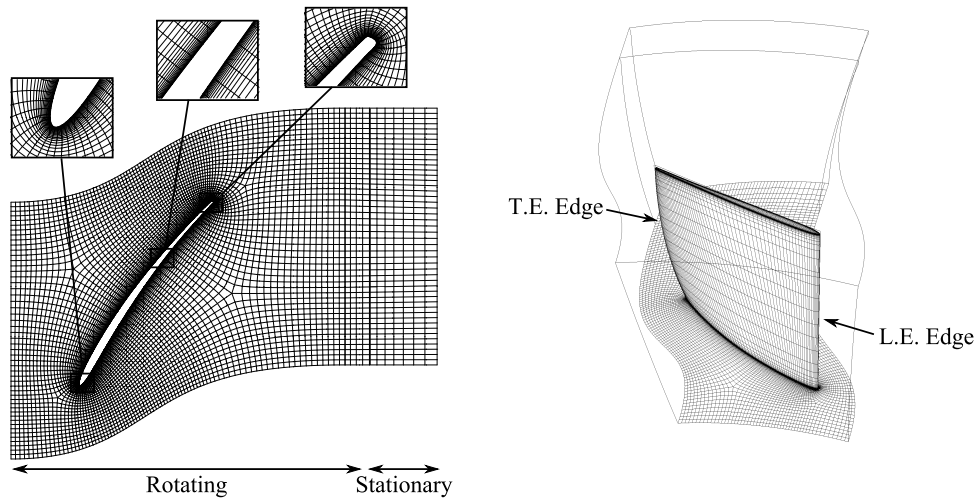


Figure 5: CFD mesh created in ANSYS Turbogrid

modelled in low Reynolds number turbomachines. The post-processing includes the calculation of the total-to-total efficiency:

$$\eta_{T/T} = \frac{\left(\frac{P_{2t}}{P_{1t}}\right)^{\frac{\gamma-1}{\gamma}} - 1}{\frac{T_{2t}}{T_{1t}} - 1} \quad (18)$$

RESULTS

This section presents the outcomes of the study carried out applying the methodology previously explained. It comprises the results of the semi-analytical approach using MISES for low and high Reynolds numbers, the numerical study of the selected designs in CFD with and without a transition model and the further postprocessing of the results from MISES to get low order models for meanline correlations.

MISES Results

Two Smith diagrams were produced using the process outlined in the MISES methodology section; the first one (Fig. 6a) at a Reynolds number typical of a small compression application ($Re = 5 \cdot 10^4$) and the second one (Fig. 6b) typical of a large scale turbomachine ($Re = 5 \cdot 10^5$).

Both graphs showed that the maximum efficiency level is achieved in a similar region at high values of the flow (from 0.7 onwards) and stage loading coefficients (from 0.4 upwards and increasing with the flow coefficient). The literature usually shows a maximum of efficiency at lower flow coefficients (Hall, 2011), however those results are comprised of both a rotor and a stator, which is likely to affect the shape of the Smith diagram. The efficiency dropped drastically for values of the stage loading coefficient below around 0.2. This is due to the low flow turning of these blades, and hence very low energy transfer into the flow, while their losses were still appreciable; since the efficiency is the ratio of the two previous factors, the losses are predominant in this region. Similarly, at low flow coefficients the efficiency also decreased. High values of stage loading coefficient (mainly at low flow coefficients) were empty in the Smith diagrams; this region corresponded to highly loaded blades, especially at the hub (due to the free vortex radial design), where significant boundary layer separation caused those points to fail to converge in MISES. A more detailed explanation of compressor design at high stage loading coefficients can be found in Dickens and Day (2011).

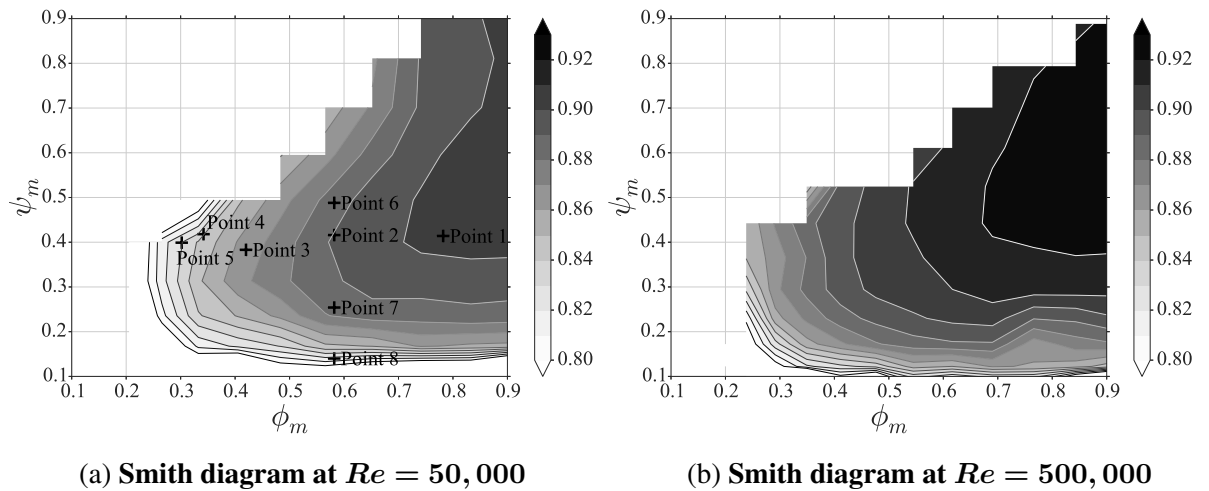


Figure 6: Comparison of Smith diagrams at low and high Reynolds numbers

The plots at high and low Reynolds numbers show a noticeable difference, the maximum efficiency level achievable at high Reynolds was higher than that at low Reynolds number; this difference was of about 2 percentage points for this study. Importantly, it can also be appreciated that the gradient of loss of efficiency towards low stage loading coefficient and low flow coefficient was steeper for the low Reynolds number machine; this means that not only were the levels of high efficiency lower for low Reynolds numbers, but also that the region of high efficiency was narrower. For example at the point ($\phi = 0.4, \psi = 0.4$), the maximum efficiency at low Re was 0.86, 4 percentage points lower than the highest efficiency on that map, whereas at high Re it was 0.89, 3 percentage points lower.

Another important difference can be seen; at high Reynolds numbers, the high efficiency contours extended towards high stage loading coefficients without any decrease. However, at low Reynolds numbers, a decrease was seen as the loading increased; this can be clearly seen at the point ($\phi = 0.6, \psi = 0.6$) where the efficiency at high Reynolds numbers was 0.91 whereas at low Reynolds numbers was 0.85. This highlights the difficulty low Reynolds number machines have while operating at high stage loading coefficients with high efficiency.

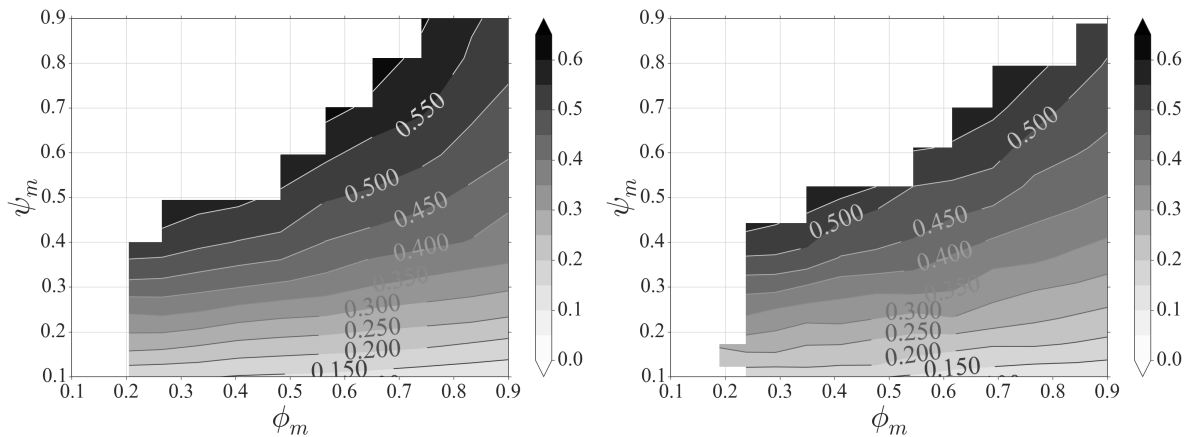
As explained before, a filter was employed to select the highest efficiency designs. From these optimum designs, the contours of optimum diffusion factor (DF) at the midspan were plotted in a similar fashion to the Smith diagram (Fig. 7).

$$DF = 1 - \frac{M_2^r}{M_1^r} + \frac{|\sin \beta_1 - (M_2^r/M_1^r) \cdot \sin \beta_2|}{2\sigma} \quad (19)$$

The DF was deemed an appropriate parameter to investigate because it illustrates the blade loading. Interestingly, the DF contours at both low and high Reynolds numbers appeared to be very similar. The main difference was at high flow coefficients, where the optimum DF was higher at low Reynolds numbers. The diffusion factor grows as the stage loading increases, showing that the location of the design on the Smith diagram determines the optimum blade diffusion factor.

CFD Results

Several points on the low Reynolds Smith diagram (Fig. 6a) were selected for further numerical validation. The procedure employed is outlined in the CFD Methodology section.



(a) Contours of optimum DF at $Re = 50,000$ (b) Contours of optimum DF at $Re = 500,000$

Figure 7: Comparison of optimum midspan DF at low and high Reynolds numbers

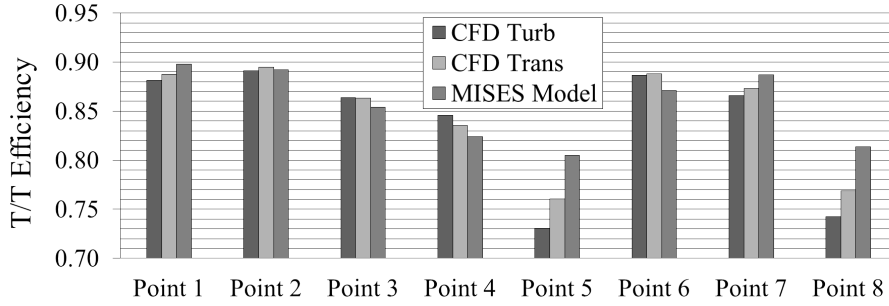


Figure 8: **Total-to-total efficiency comparison of the CFD turbulence model, CFD transition model and semi-analytical model at $Re = 50,000$**

Fig. 8 shows the comparison between the CFD simulations (with and without a transition model) and the model developed in the current paper. The efficiency calculated by the model was between $\pm 2\%$ of efficiency compared to the CFD results, except for point 5 and point 8, which are points located in regions of low total-to-total efficiency. The two different CFD models showed very similar results as well, with the exception of the same two points. The points of study on the Smith diagram have been selected roughly along a line of constant stage loading coefficient ($\psi = 0.4$) and a line of constant flow coefficient ($\phi = 0.6$).

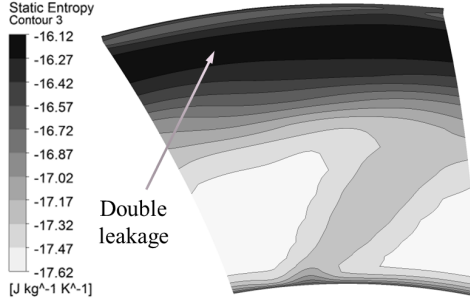
Beginning with the line of constant stage loading coefficient (points 1-5), the CFD simulations predicted a maximum of efficiency at point 2 as opposed to the model which showed that the maximum efficiency was achieved at higher flow coefficients (point 1). Nevertheless, continuing towards lower flow coefficients, the semi-analytical model captures the trend of dropping efficiency; the gradient from point 4 to point 5 is however steeper in CFD.

The line of constant flow coefficient (points 6, 2, 7 and 8) showed maximum efficiency at point 2 both in the model and in CFD. The efficiency dropped as the stage loading coefficient decreased as discussed previously and again this gradient was steeper in CFD than in the model (point 7 to point 8).

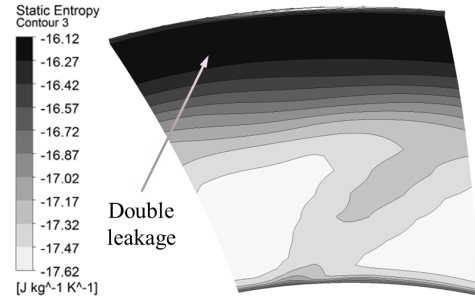
The main difference observed was that the model overpredicted the efficiency for points 5 and 8. These points also corresponded to significant differences in the prediction of efficiency between the CFD simulations with and without a transition model of around 3%. A closer look into the CFD results showed that the differences stemmed from very different phenomena.

Firstly, point 5 was investigated. Fig. 9 displays an entropy contour plot on a constant axial location plane placed just upstream of the mixing plane. The plot showed a wide region of high entropy at the tip, which was produced by the tip leakage. Due to the low flow coefficient and hence high stagger angle of the blade, the axial fan presented the phenomenon called double leakage (Khalsa, 1996), which has been reported to increase tip leakage losses and flow blockage (Borislav, 2001). The model developed in this paper breaks down when the flow becomes highly 3D and was not able to capture the increased losses and blockage associated with double leakage. However, it was able to capture the drop in efficiency towards lower flow coefficients.

Furthermore, in order to understand the efficiency difference between the CFD simulations with and without transition models, the surface streamlines and the wall shear stress along the axial direction were investigated. Fig 10 shows the regions of attached (dark grey) and separated (light grey) boundary layer on the blade (shown by positive and negative wall shear stress along the axial direction respectively). As it can be seen, the flowfield was considerably different, with the transition model showing an important area of separated flow at the trailing edge, a feature that was not captured by the fully turbulent SST turbulence model.

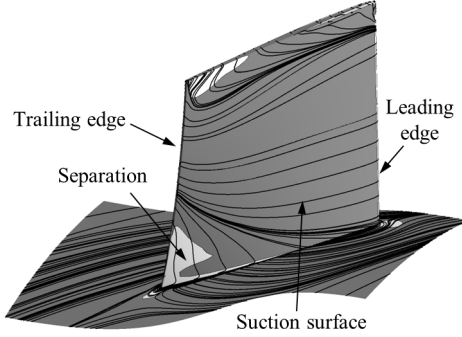


(a) $k - \omega$ SST turbulence model

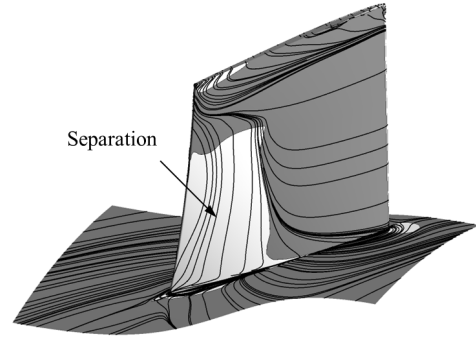


(b) $k - \omega$ SST with $\gamma - \theta$ transition model

Figure 9: **Point 5 contours of entropy on a constant axial location plane located upstream of the mixing plane at $Re = 50,000$**



(a) $k - \omega$ SST turbulence model



(b) $k - \omega$ SST with $\gamma - \theta$ transition model

Figure 10: **Point 5 surface streamlines on the fan hub and blade. Regions of attached (dark grey) and separated (light grey) boundary layer on the blade (shown by positive and negative wall shear stress along the axial direction) at $Re = 50,000$**

The differences seen between the various models at point 8 (Fig. 8) were due to a different effect to point 5. As can be seen in Fig. 6, point 8 corresponded to a region of steep efficiency gradient on the Smith diagram. As the loading at this point was relatively low, small differences of computed loss coefficient and deviation substantially affected the calculated efficiency.

Low-order modelling

As part of the model validation, typical axial fan meanline correlations and historical data were calculated and compared with the data extracted from the 2D simulations in MISES. These were namely the loss coefficient and the flow deviation. Results at both high and low Reynolds numbers were compared and the differences highlighted.

Lieblein (1965) defined a modified loss coefficient (ω^*):

$$\omega^* = \frac{\omega \cos \beta_2}{2\sigma} \left(\frac{\cos \beta_2}{\cos \beta_1} \right)^2 \quad (20)$$

The diffusion factor (DF , Eq. 19) and the modified loss coefficient (ω^*) obtained from MISES simulations were plotted along with historical experimental data from the report NASA SP-36 (Lieblein, 1965) carried out at $Re = 245,000$ (Fig. 11). MISES datasets at low and high Reynolds numbers were fitted with a range of regressional models, with an exponential curve

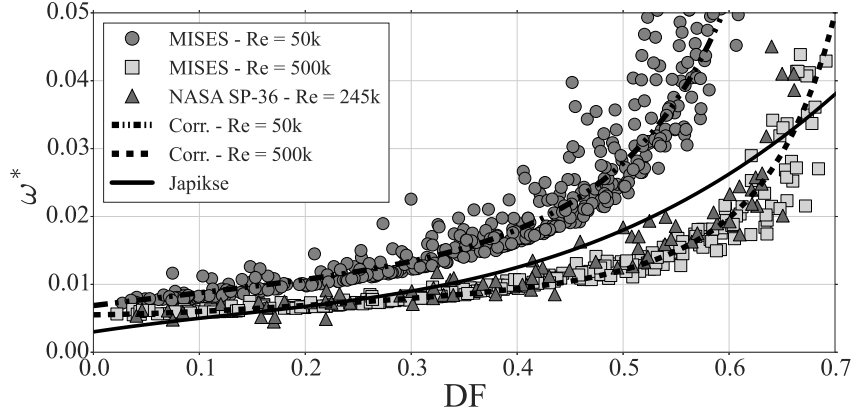


Figure 11: **Modified loss coefficient variation vs diffusion factor at different Re numbers**

best fitting the available data. These curves were overlaid on the same graph together with the polynomial fit of Lieblein's data provided in Japikse and Baines (1997):

$$\omega_{LowRe}^* = \exp^{-4.98+2.8DF-4.8DF^2+9.6DF^3} \quad (21)$$

$$\omega_{HighRe}^* = \exp^{-5.2+0.3DF+7.6DF^2-22.7DF^3+25.2DF^4} \quad (22)$$

$$\omega_{Japikse}^* = 0.003 + 0.02375DF - 0.05DF^2 + 0.125DF^3 \quad (23)$$

The results shown in Fig. 11 revealed that NASA's experimental data ($Re = 245,000$) and the high Reynolds number calculations ($Re = 500,000$) laid relatively on top of each other with the NASA measurements showing a slightly higher loss coefficient as expected, which provided confidence in the validity of the results. The low Reynolds number simulations provided much higher loss values across all diffusion factors. It was also shown that for low Reynolds numbers, diffusion factors higher than 0.5 could not be achieved without a drastic increase on the losses; this value could be considered as a limiting factor for the design of low Reynolds number axial fans. Similarly, the plot also showed that for high Reynolds numbers, profiles exceeding a diffusion factor of 0.6 drastically increased their losses, as typically indicated in the literature (Dixon and Hall, 2010). The spread of low Reynolds numbers points around the provided exponential fit is of around $\pm 15\%$ up to a diffusion factor of 0.5, increasing from that point onwards.

Furthermore, the flow deviation simulated in MISES (δ_{MISES}) was compared to the deviation calculated using the correlation given by the Carter's rule (δ_{CARTER}) from Poniatowski (1988).

$$\delta_{MISES} = \beta_2 - \chi_2 \quad (24)$$

$$\delta_{CARTER} = \frac{(0.23 + 0.002 \cdot \beta_2) \Delta \chi}{\sigma^{0.5}} \quad (25)$$

Fig. 12 shows the comparison of the two magnitudes. The solid line represents the equivalence between simulations and Carter's rule, the dashed lines have been plotted above and below one degree on either side of the solid line. Fig. 12 showed that Carter's rule predicted the deviation of high Reynolds number profiles within about ± 2 degrees, however it underpredicted the deviation values at low Reynolds numbers, especially when the deviation was high. This result highlighted the higher deviation that profiles suffer at low Reynolds numbers compared to when they operate at high Reynolds numbers.

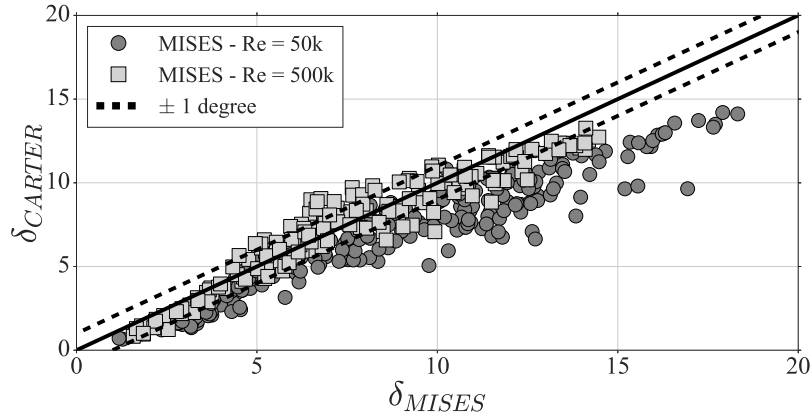


Figure 12: Comparison of calculated deviation in MISES and prediction of Carter's rule

CONCLUSIONS

This paper investigates the effect of Reynolds number on the Smith diagram of a subsonic axial fan rotor. To that end, a semi-analytical approach was considered and the results further validated using CFD simulations with and without a transition model.

Smith diagrams at high ($5 \cdot 10^5$) and low ($5 \cdot 10^4$) midspan chord-based Reynolds numbers showed regions of high efficiency at the same region of flow coefficient over 0.7 and stage loading coefficient over 0.4. Maximum achievable efficiencies at high Reynolds numbers were 2% higher than those calculated at low Reynolds numbers. The drop of efficiency towards both low stage loading coefficients and low flow coefficients was much steeper at low Reynolds numbers. High Reynolds numbers axial rotor fans also exhibited a much broader region of high efficiency compared to low Reynolds numbers.

The location of the design on the Smith diagram determines the optimum blade diffusion factor. Contours of the optimum diffusion factor were plotted in a similar manner to the Smith diagram, showing a very similar distribution at low and high Reynolds numbers. At high flow coefficients, the optimum diffusion factor at low Reynolds numbers was slightly higher than at high Reynolds numbers.

CFD simulations with and without a transition model were carried out and their results compared against the model for several points on the low Reynolds Smith diagram. Good agreement between CFD simulations and the model was achieved. Both datasets followed the same trend, however CFD predicted maximum efficiency at a slightly lower flow coefficient and a much steeper drop off in efficiency towards both low flow coefficients and stage loading coefficients. The CFD simulations with and without a transition model showed similar values of efficiency, except at low flow coefficients and low stage loading coefficients, where the difference was approximately 3%. These regions also presented the maximum difference between CFD and the developed model. The reasons for the discrepancy were explained based on the CFD results.

Results extracted from MISES simulations were plotted in terms of the diffusion factor and the modified loss coefficient. High Reynolds numbers simulations matched historical experimental results from NASA SP-36. Low Reynolds numbers results do not overlay with the previous NASA high Reynolds data. Several trendlines that better follow the high and low Reynolds number data were developed.

Calculations of the profile deviation using Carter's rule were compared to the simulations in MISES. Carter's rule underpredicted deviation especially at high deviation values and low Reynolds numbers.

ACKNOWLEDGEMENTS

The authors wish to thank Dyson for permitting the publication of this paper.

REFERENCES

- Borislav, T.D. (2001). Effect of Upstream Unsteady Flow Condition on Rotor Tip Leakage Flow. Master's thesis, MIT.
- Casey, M.V. (1985). The Effects of Reynolds Number on the Efficiency of Centrifugal Compressor Stages. *Journal of Engineering for Gas Turbines and Power*, 107(2), pages 541–548.
- Denton, J.D. (1993). Loss Mechanisms in Turbomachines. *ASME International Gas Turbine and Aeroengine Congress and Exposition*.
- Dickens, T. and Day, I. (2011). The Design of Highly Loaded Axial Compressors. *Journal of Turbomachinery*, 133(3).
- DiOrio, A.G. (2012). Small Core Axial Compressors for High Efficiency Jet Aircraft. Master's thesis, MIT.
- Dixon, S.L. and Hall, C.A. (2010). *Fluid Mechanics and Thermodynamics of Turbomachinery - 6th edition*. Elsevier Inc.
- Drela, M. and Youngren, H. (2008). *A User's Guide to MISES 2.63*. MIT Aerospace Computational Design Laboratory.
- Fitzgerald, N.A. (2002). Probabilistic Analysis of Meanline Compressor Rotor Performance. Master's thesis, MIT.
- Gray, J., Moore, K.T., and Naylor, B.A. (2010). OpenMDAO: An Open Source Framework for Multidisciplinary Analysis and Optimization. *13th AIAA/ISSMO Multidisciplinary Analysis and Optimization Conference Proceedings, Texas*.
- Hall, D.K. (2011). Performance Limits of Axial Turbomachine Stages. Master's thesis, MIT.
- Japikse, D. and Baines, N.C. (1997). *Introduction to Turbomachinery*. Concepts ETI, Inc. and Oxford University Press.
- Khalsa, A.S. (1996). *Endwall Blockage in Axial Compressors*. PhD thesis, MIT.
- Kulfan, B.M. and Bussolletti, J.E. (2006). "Fundamental" Parametric Geometry Representations for Aircraft Component Shapes. *11th AIAA/ISSMO Multidisciplinary Analysis and Optimization Conference, Virginia*.
- Lieblein, S. (1965). Experimental Flow in Two-Dimensional Cascades. Chapter VI in Aerodynamic Design of Axial-Flow Compressors. Technical report, NASA SP-36.
- Maffioli, A., Hall, C., and Melvin, S. (2015). Aerodynamics of Low Reynolds Number Axial Compressor Sections. *53rd AIAA Aerospace Sciences Meeting, Florida*.
- Pelz, P.F. and Stonjek, S.S. (2013). The Influence of Reynolds Number and Roughness on the Efficiency of Axial and Centrifugal Fans - A Physically Based Scaling Method. *Journal of Engineering for Gas Turbines and Power*, 135(5).
- Poniatowski, E.M. (1988). The Effects of Incidence Angle and Free Stream Turbulence on the Performance of a Variable Geometry Two-Dimensional Compressor Cascade at High Reynolds Numbers. Master's thesis, Air Force Institute of Technology.
- Schreiber, H.A., Steinert, W., Sonoda, T., and Arima, T. (2004). Advanced High-Turning Compressor Airfoils for Low Reynolds Number Condition - Part II: Experimental and Numerical Analysis. *Journal of Turbomachinery*, 126(4), pages 482 – 492.